Exp Fluids (2012) 52:1307–1318
DOI 10.1007/s00348-011-1257-1

RESEARCH ARTICLE

Estimating void fraction in a hydraulic jump by measurements of pixel intensity

J. Leandro · R. Carvalho · Y. Chachereau · H. Chanson

Received: 15 November 2010 / Revised: 18 November 2011 / Accepted: 20 December 2011 / Published online: 3 January 2012

Abstract A hydraulic jump is a sudden transition from supercritical to subcritical flow. It is characterized by a highly turbulent roller region with a bubbly two-phase flow structure. The present study aims to estimate the void fraction in a hydraulic jump using a flow visualization technique. The assumption that the void fraction in a hydraulic jump could be estimated based on images' pixel intensity was first proposed by Mossa and Tolve (J Fluids Eng 120:160–165, 1998). While Mossa and Tolve (J Fluids Eng 120:160–165, 1998) obtained vertically averaged air concentration values along the hydraulic jump, herein we propose a new visualization technique that provides air concentration values in a vertical 2-D matrix covering the whole area of the jump roller. The results obtained are found to be consistent with new measurements using a dual-tip conductivity probe and show that the image processing procedure (IPP) can be a powerful tool to complement intrusive probe measurements. Advantages of the new IPP include the ability to determine instantaneous and average void fractions simultaneously at different locations along the hydraulic jump without perturbing the flow, although it is acknowledged that the results are likely to be more representative in the vicinity of sidewall than at the center of the flume.

J. Leandro (✉) · R. Carvalho
IMAR-CMA, Department of Civil Engineering,
Faculty of Science and Technology, University of Coimbra,
Rua Luís Reis Santos, Pólo II, 3030-788 Coimbra, Portugal
e-mail: leandro@dec.uc.pt

Y. Chachereau · H. Chanson
School of Civil Engineering, The University of Queensland,
Brisbane, QLD 4072, Australia

Abbreviations

a, b	Parameters of the Fuzzy logic S function
C	Void fraction defined as the volume of air per unit volume of air and water; it is also called air concentration
$AvPI$	Averaged pixel intensity matrix (pi)
$AvPIt$	Time average matrix (pi)
Fr	Froude number
g	Acceleration due to gravity: g = 9.81 m^2/s
h_1	Upstream water depth (m)
i, j	Matrix indexes
I_{T1}, I_{T2}, I_{T3}	Thresholding functions
$limS$	Water surface upper limit (i)
$limSt$	Water surface lower limit (i)
lmf	Fuzzy logic linear function
n, m	Matrix dimensions
p, q	Factors of m and n
pi	Pixel intensity defined as a single point in a gray scale image; pi = 0 for a black pixel and pi = 255 for a white pixel
$PI_{i,j}$, $PI_{i,j}^{1...4}$	Matrices of pixel intensity (pi)
$PI_{i,j}^{f}$	Transformed matrix (pi)
Ptr, $Ptr2$	Threshold values (pi)
Q	Flow rate (l/s)
Re	Reynolds number
RPI	Resized pixel intensity matrix (pi)
$RPI(:,:)_{i,j}$	(i, j)th submatrix of RPI (pi)
Smf	Fuzzy logic S function
U_1	Upstream mean velocity (m/s)
x_1	Horizontal distance between the gate and the jump toe (m)
$x - x_1$	Horizontal distance between the jump toe and the conductivity probe (m)
x, y	Horizontal and vertical coordinates (m)

y_1, y_2	Parameters of the Fuzzy logic linear function
Y_{90}	Characteristic depth (m) where air concentration is 90%
We	Weber number

Greek symbols

Δx, Δy	Horizontal and vertical grid resolution (pi)
δ	Boundary layer thickness (m)
Ø	Diameter (m)

1 Introduction

A hydraulic jump is a rapid transition from supercritical to subcritical flow, which can be found in both natural and man-made open channel flows. It is characterized by the formation of a surface roller associated with air entrainment, turbulence, and energy dissipation. The water depth downstream of the jump can be predicted by the Bélanger equation based on the upstream depth and inflow Froude number defined as $Fr_1 = U_1/\sqrt{g \times h_1}$, where U_1 is the upstream mean velocity, h_1 is the upstream water depth, and g is the acceleration due to gravity. Figure 1 shows a sketch with notation. The study of hydraulic jumps is a subject of utmost interest to engineers as energy dissipators as well as for self-aeration: for example, at dam spillways, riverine and coastal applications, water treatment works.

Despite the extensive literature on the macroscopic features of the hydraulic jump, many characteristics of its internal flow remain unanswered (Carvalho et al. 2008; Mccorquodale and Khalifa 1983). Carvalho et al. (2008) argued that the highly variable mixture of air–water flow in hydraulic jumps in both space and time creates difficulties to laboratory measurements of flow properties inside strong hydraulic jumps ($Fr_1 > 5$). Using laser Doppler anemometry (LDA), Long et al. (1990) reported low rates of data acquisition whenever air bubbles were present, while

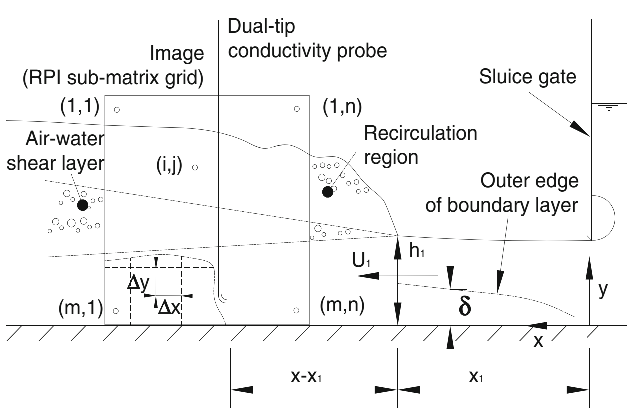

Fig. 1 Definition sketch of a hydraulic jump, dual-tip conductivity probe, and image location

Qingchao and Drewes (1994) found a scattered bubbles frequency distribution. Carvalho (2002) showed that acoustic Doppler velocimetry (ADV) becomes unstable in the presence of high air–water contents. Average flow velocity measurements using Prandtl-pitot, and instantaneous measurements using ADV, were reported, however, away from high air–water mixtures areas (Carvalho 2002). Resch and Leutheusser (1972) reported successfully instantaneous flow velocity measurements using hot-film anemometer techniques.

Air concentration or void fraction is defined as the ratio of the volume of air to the volume of air and water in a small volume at a given point. Rajaratnam (1962) was one of the first to measure air concentration using electric-resistive probes. Resch et al. (1974) used hot-film anemometry with conical probes to record void ratio and bubble size in a hydraulic jump, while Chanson (2007) and Chanson and Brattberg (2000) used single-tip and dual-tip conductivity probes. Murzyn et al. (2005), Murzyn and Chanson (2008) and Chanson and Carosi (2007) used dual-tip probe optical phase detection for measuring void fractions, bubble frequencies, and sizes. All previous studies shared in common the use of intrusive probes to determine void fraction, except for the work of Mossa and Tolve (1998) in which visualization techniques were used to indirectly estimate air concentration. Mossa and Tolve (1998) estimated vertical averaged air concentration along a hydraulic jump and compared their data with an empirical law based on Rajaratnam's (1962) experimental data. Their test results used ten snapshots taken from an interval of 1.5 s, where each snapshot was divided into six regularly spaced intervals to characterize the mean vertical values.

The aim of the present study is to estimate the instantaneous and time-averaged void fraction data in a hydraulic jump based upon a visualization technique. The experimental facility is presented in Sect. 2 along with instrumentation specifications (probe and camera) and flow conditions. Section 3 describes the image processing procedure. Section 4 compares and discusses the void fraction results with measurements using the dual-tip conductivity probes.

2 Experimental set-up and flow conditions

The experiments were carried out in a horizontal rectangular channel at the University of Queensland (UQ). The channel was 0.50 m wide, with 0.45 m deep, and 3.2 m long glass sidewalls. An upstream sluice gate controlled the formation of the hydraulic jump. The validation data set was collected using a dual-tip conductivity probe (sensor Ø 0.25 mm) manufactured at UQ, based on the principle of resistance difference between air and water. Further details on the channel and probes can be found in Chanson (2007), Kucukali and Chanson (2008), and Chachereau and Chanson (2011). The data collected consisted of vertical profiles of void fraction sampled at 20 kHz for 45 s at different cross-sections along the hydraulic jump on the channel centerline. Each profile contained at least 25 points.

Some mere geometrical optical considerations show that, when a ray of light travels through a liquid, it does not change its direction and intensity. However, when it intercepts a transparent air bubble, the ray intensity drops along the incident direction because of three mechanisms: reflection, refraction, and diffraction (Davoust et al. 2002). Our aim is to set-up the experiment similar to the one in the work of Mossa and Tolve (1998) in order to capture with a photographic camera the light changes induced by three mechanisms when air bubbles are present in the flow.

The image acquisition used a Pentax™ K-7 camera equipped with a Voigtlander™ Nokton 58 mm lens set for ISO-800, F-stop f/1.4 with less than 0.1% of distortion over the entire focal length, and camera frame rate of 5.2 frames per second (5.2 fps). Exposure time was set to 1/500 s and image dimensions to 3,072 × 2,048 pixels. The camera was switched to manual mode to keep the same light exposure throughout the image collection. A white piece of paper was installed in an area close to the hydraulic jump to check the consistency of the images' light exposure. The background was covered with black sheets to minimize reflection and prevent background lights to affect the camera readings. In addition, all tests were conducted with daylight uniform conditions, that is, within a short period of time to ensure diffused light and to guarantee that all images were taken with same light intensity.

Alike particle image velocimetry (PIV) or bubble image velocimetry (BIV) methods (Lennon and Hill 2006; Ryu et al. 2005), the method proposed herein is not able to measure the component along the axis perpendicular to the camera. In aerated areas, only BIV (out of the two methods mentioned) can be applied and typically in the vicinity of the sidewalls. In this case, the bubbles velocity is tracked without a laser light illumination, while the error is minimized by limiting the depth of field (DOF). Bubbles outside the DOF are expected to have insignificant influence, because the intensity of the bubbles is much weaker than the ones inside the DOF (Ryu et al. 2005). It is, however, acknowledged that BIV data might be adversely affected by sidewall effects. Furthermore (and alike BIV), the focal plane cannot be set at the channel centerline because of the shadow effect caused by the forefront air bubbles. Thus, the photographs were taken with the camera focal point set at 5 mm from the inner sidewall with a limited DOF of 20 mm; the conductivity probe measurements were taken on the channel centerline (CL) and not at 5 mm from the wall, in order to avoid errors in the measurements due to splashes near the sidewall (Kucukali and Chanson 2008) and possible enhancement/interference with the sidewall effects.

The experimental flow conditions are summarized in Table 1, where the test number describes the experimental run, Q is the flow rate, Re is the Reynolds number, We is the Weber number, x_1 is the horizontal distance between the gate and the jump toe, and $x - x_1$ is the horizontal distance between the jump toe and the conductivity probe. The corresponding Reynolds numbers and Weber numbers (Table 1) were large enough to minimize scale effects and neglect surface tensions (Murzyn and Chanson 2008). For all experiments, the inflow conditions were partially developed ($\delta/h_1 < 0.4$) (Chachereau and Chanson 2011).

3 Image processing procedure

The image processing aims to determine the instantaneous void fraction time series and time-averaged values in the hydraulic jump roller. Our hypothesis is that the void fractions can be estimated based on images' pixel intensity (pi). The image processing procedure consists of two algorithms written in Matlab: (1) Image Editing (IE) and (2) Pixel Intensity Matrix (PIM) algorithms. Both algorithms and subfunctions are run for all images.

The first algorithm is of uppermost importance because it allows the calibration of the image processing procedure (IPP) using the data collected with the dual-tip conductivity probes. Indeed, any technique using images as input must resort to a calibration algorithm to account for the subtleties of a particular site light exposure which might vary with the testing site location and facility. The second algorithm calculates the averaged pixel intensity matrix $AvPI$ necessary for calculating the vertical profiles of time-averaged void fraction (Fig. 1).

Table 1 Summary of the experimental flow conditions in the hydraulic jumps

Test	Q (l/s)	U_1 (m/s)	h_1 (mm)	Fr_1	Re	We	x–x_1 (m)
T1.1	54.5	3.03	39.5	4.4	1.1E+5	4.8E+4	0.15
T1.2							0.30
T1.3							0.45
T2.1	62.7	3.48	39.5	5.1	1.2E+5	6.9E+4	0.15
T2.2							0.30
T2.3							0.45

3.1 Image Editing (IE)

Fuzzy logic has been widely applied in image processing since L. Zadeh introduced it in 1965. Its application range from general image contrast enhancement (Vorobel and Berehulyak 2006) to specific color enhancements (Sarode et al. 2008). Earlier tests using the Pixel Intensity Matrix (PIM) algorithm in this experiment showed that it could not explain on its own the air concentration profiles recorded with the dual-tip conductivity probe. Hence, an algorithm was sought to enhance the images' contrast before calibration and validation. The Image Editing (IE) algorithm is built based upon concepts found in Fuzzy inference systems, such as membership functions, thresholding, and if–then rules as defined in Bezdek et al. (1999). These functions enhance the image contrast by assigning a transformed value at every given pixel (i, j).

The black boards placed behind the experiment (described in previous section) generate images that display two distinct areas divided by the water surface: the area above the water surface where black pixels represent points with 100% of air concentration and the area below the water surface where gray pixels represent points with air concentration less than 100%. Because of the unsteady nature of the water surface, it is not possible to define a clear boundary between these two areas. In addition, given that a black pixel has a pixel intensity pi = 0 and a white pixel pi = 255, the Image Editing algorithm has to distinguish between the black pixel above the water surface (100% air) and a black pixel below the water surface (0% air).

The pixel intensity (pi) values are obtained by transforming the RGB images into gray scale images using a Photoshop™ built-in function. Each image is defined by a bi-dimensional matrix of pixel intensity, $PI_{i,j}$, with values ranging from 0 to 255, ($m \times n$) dimensions, and row and column defined by i and j indexes, respectively (Fig. 2).

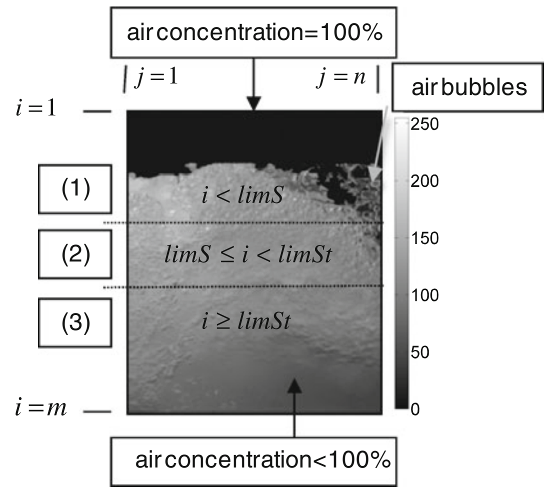

Fig. 2 Definition of the *gray scale* image areas: *1* above the water surface, *2* transitional area, and *3* below the water surface, according with the image row index i and for $m = 960$ and $n = 800$

The IE algorithm works by running all the values stored within each image, that is, the $PI_{i,j}$ matrix and converts it into a new image $PI^f_{i,j}$, the transformed matrix. Equation 1 defines the IE algorithm:

$$PI^f_{i,j} = \begin{cases} \underbrace{I_{T3}(PI_{i,j}) \times PI^3_{i,j}}_{\substack{\text{LinearTransition}\left(PI_{i,j}-PI^1_{i,j}\right)\\ \text{for}(i<\lim S)}} + \underbrace{I_{T2}(PI_{i,j}) \times PI^2_{i,j}}_{\text{Lighten}\left(PI_{i,j}\right)}, & i < \lim S \\ \underbrace{I_{T3}(PI_{i,j}) \times I_{T1}(PI_{i,j}) \times PI^1_{i,j}}_{\text{Darken}\left(PI_{i,j}\right)} + \underbrace{I_{T1}(PI_{i,j}) \times I_{T2}(PI_{i,j}) \times PI^4_{i,j}}_{\substack{\text{LinearTransition}\left(PI^1_{i,j}-PI^2_{i,j}\right)\\ \text{for}(\lim S\leq i<\lim St)}}, & \lim S \leq i < \lim St \\ \underbrace{I_T(PI_{i,j}) \times PI^1_{i,j}}_{\text{Darken}\left(PI_{i,j}\right)}, & i \geq \lim St \end{cases} \quad (1)$$

Equation 1 is the main function used to edit the image area above (top equation) and below the water surface (bottom equation) as well as in the transitional area (middle equation). In Eq. 1, $PI^n_{i,j}$ is the nth editing of $PI_{i,j}$ and I_{Tn} is the nth thresholding function used for the editing calibration (see below).

Since the IE algorithm must distinguish the three mentioned areas (Fig. 2), an if–then rule is constructed imposing a water surface lower (*limSt*) and upper (*limS*) limit. With these two limits, the three areas can be clearly identified as: (1) the area below the water surface identified by $i \geq limSt$, (2) the area above the water surface identified by $i < limS$, and (3) the transitional area identified by $limS \leq i < limSt$. The definition of the transitional area is justified by the complex air–water interface nature of the hydraulic jump discussed by Mouaze et al. (2005), making impossible a clear definition of the water surface boundary (Misra et al. 2006; Murzyn and Chanson 2009).

For the sake of clarity, we will first introduce the subfunction that deals with the area below the water surface (IE-step 1), followed by the subfunction defined for the area above the water surface (IE-step 2), and conclude with the subfunction for the transitional area (IE-step 3). Figure 3 illustrates the three steps in the IE algorithm corresponding to the three subfunctions in Eq. 1.

3.1.1 *IE-step 1*

In Fig. 2, the dark gray areas below the water surface must have an air concentration close to 0, while lighter area must have values greater than 0. The main objective of the subfunction defined for the area below the water surface is to darken the areas with low pi while keeping the lighter areas, with higher pi, unchanged. This can be achieved with the use of the Fuzzy logic S function (Vorobel and Berehulyak 2006). Equation 2 defines the *Smf* membership function:

$$Smf(x,[a,b]) = \begin{cases} 0, & x \le a \\ 2\left(\frac{x-a}{b-a}\right)^2, & a < x \le \frac{a+b}{2} \\ 1-2\left(\frac{x-b}{b-a}\right)^2, & \frac{a+b}{2} < x \le b \\ 1, & x > b \end{cases} \tag{2}$$

In the literature, $(a + b)/2$ is called the cross-over point, meaning that x values above it have membership greater than 0.5 and values below it have membership values less than 0.5. In Eq. 2, $x = PI_{i,j}$ and the cross-over point equal the midpoint of the gray scale. Thus, the minimum and maximum limits become equal to $a = 0$ and $b = 255$, respectively. The *Smf* membership function varies between 0 and 1; therefore, in order to obtain the first edited image $PI^1_{i,j}$, one needs to multiply the *Smf* by the original image. This yields Eq. 3:

$$PI^1_{i,j} = PI_{i,j} \times Smf\left(PI_{i,j},[0,255]\right) \tag{3}$$

Because IE-step1 specifies the limits of the *smf* function, a segmentation-via-thresholding function is applied to the resulting image $PI^1_{i,j}$ with the purpose of providing a calibration parameter to the IE algorithm. Eq. 4 defines the thresholding function:

$$I_{T1}(x) = \begin{cases} 1, & x \ge Ptr \\ 0, & x < Ptr \end{cases} \tag{4}$$

where Ptr represents the first threshold value. Equation 5 then defines the final subfunction used for the area below the water surface.

$$PI^f_{i,j} = \underbrace{I_{T1}(PI_{i,j}) \times PI^1_{i,j}}_{\text{Darken}\left(PI_{i,j}\right)} \tag{5}$$

3.1.2 *IE-step 2*

The area above the water level (Fig. 2) shows a top black area of 100% air concentration as well as air bubbles attached to the glass wall with very low pi (close to 0). Having in mind the hypothesis stated earlier, the IE algorithm needs first to alter the top black area pi to complete white and second to eliminate the (darker) air bubbles that remain attached to the wall in order to avoid an under-prediction of the air concentration. This is done with a Fuzzy logic linear function in which limits have been adapted for easiness of implementation. Equation 6 defines the *lmf* membership function:

$$lmf(x,[a,b,y_1,y_2]) = \begin{cases} y_2, & x \le a \\ \frac{y_2-y_1}{a-b}x + \frac{y_1 a - y_2 b}{a-b} & a \le x \le b \\ y_1, & x \ge b \end{cases} \tag{6}$$

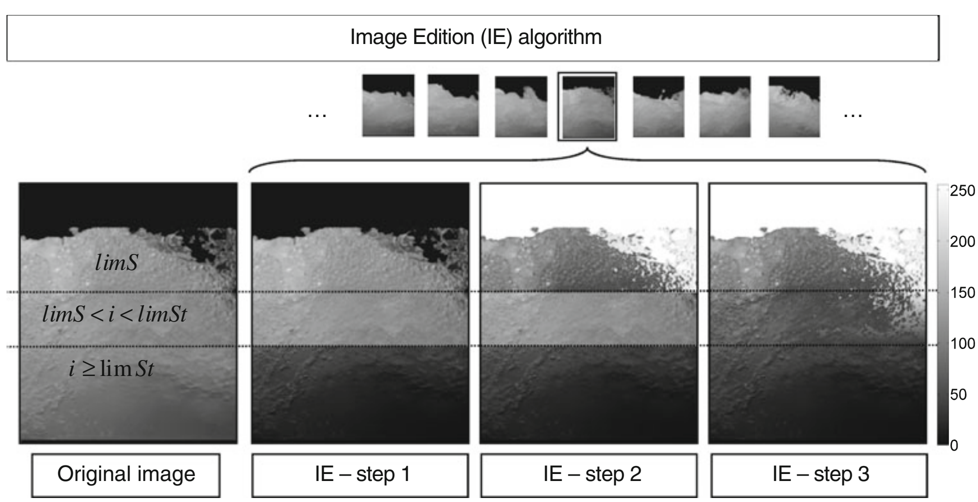

Fig. 3 Definition of the three steps in the Image Edition algorithm ($m = 960$, $n = 800$): IE-step 1 (edition of the area *below* water surface), IE-step 2 (edition of the area *above* the water surface), and IE-step 3 (edition of the transitional area)

where these limits are changed to vary linearly between y_1 and y_2, instead of having membership values limited between 0 and 1. Herein, y_2 is set to the gray scale maximum limit 255 (complete white) and y_1 is set to 180. y_1 is defined with a fixed value always greater than the pi of darker air bubbles. (A second calibration parameter of IE is only defined later with the introduction of two more segmentation-via-thresholding functions.) Hence, the transformed image can be directly obtained with Eq. 7:

$$PI^2_{i,j} = lmf\left(PI_{i,j}, [Ptr, 180, 180, 255]\right) \tag{7}$$

To keep a smooth transition between the original image and the transformed image obtained in IE-step 1 $PI^1_{i,j}$, a third transformed image is required. Equation 8 defines the third transformed image. Thus, unlike Eq. 7, the image is now transformed as a function of the vertical coordinate (i), setting the values of a and b to 1 and $limS$, respectively:

$$PI^3_{i,j} = lmf\left(i, \left[1, limS, PI^1_{i,j}, PI_{i,j}\right]\right) \tag{8}$$

Finally, two complementary segmentation-via-thresholding functions are applied to the resulting images, with the purpose of providing a second calibration parameter to the IE algorithm by changing the weight of the two transformed images. Equations 9 and 10 define the two extra thresholding functions:

$$I_{T2}(x) = \begin{cases} 1, & x \leq Ptr2 \\ 0, & x > Ptr2 \end{cases} \tag{9}$$

$$I_{T3}(x) = \begin{cases} 1, & x > Ptr2 \\ 0, & x \leq Ptr2 \end{cases} \tag{10}$$

where $Ptr2$ represents the second threshold value. Equation 11 defines the final subfunction used for the area above the water surface:

$$PI^f_{i,j} = \underbrace{I_{T3}(PI_{i,j}) \times PI^3_{i,j}}_{\substack{\text{Linear Transition}\left(PI_{i,j}-PI^1_{i,j}\right) \\ \text{for}(i<limS)}} + \underbrace{I_{T2}(PI_{i,j}) \times PI^2_{i,j}}_{\text{Lighten}\left(PI_{i,j}\right)} \tag{11}$$

3.1.3 *IE-step 3*

The transitional area is necessary for providing a gradual transition between the transformed images above and below the water surface while keeping the aim in IE-step 1, that is, darkening the areas with low pi value and keeping the lighter areas unchanged. Hence, we recover the subfunction used in IE-step 1 (left expression in Eq. 13) and the *lmf* membership function to apply a linear transition between the transformed images in IE-step 1 $PI^1_{i,j}$ and IE-step 2 $PI^2_{i,j}$. Equation 12 defines the fourth transformed image, and Eq. 13 defines the final subfunction used for the transitional area:

$$PI^4_{i,j} = lmf\left(i, \left[limS, limSt, PI^2_{i,j}, PI^1_{i,j}\right]\right) \tag{12}$$

$$\begin{aligned} PI^f_{i,j} = {} & \underbrace{I_{T3}(PI_{i,j}) \times I_{T1}(PI_{i,j}) \times PI^1_{i,j}}_{\text{Darken}\left(PI_{i,j}\right)} \\ & + \underbrace{I_{T1}(PI_{i,j}) \times I_{T2}(PI_{i,j}) \times PI^4_{i,j}}_{\substack{\text{Linear Transition}\left(PI^1_{i,j}-PI^2_{i,j}\right) \\ \text{for}(limS \leq i < limSt)}} \end{aligned} \tag{13}$$

3.2 Pixel Intensity Matrix (PIM)

The Pixel Intensity Matrix (PIM) aim is to calculate the pixel intensity average matrix over time, used to predict the air concentration at any given point within each image $PI^f_{i,j}$. For the sake of simplicity, from this point onwards, these images will be referred to as PI. The PIM algorithm is defined by three steps: PIM-step 1 divides the image into smaller matrices, PIM-step 2 calculates the average

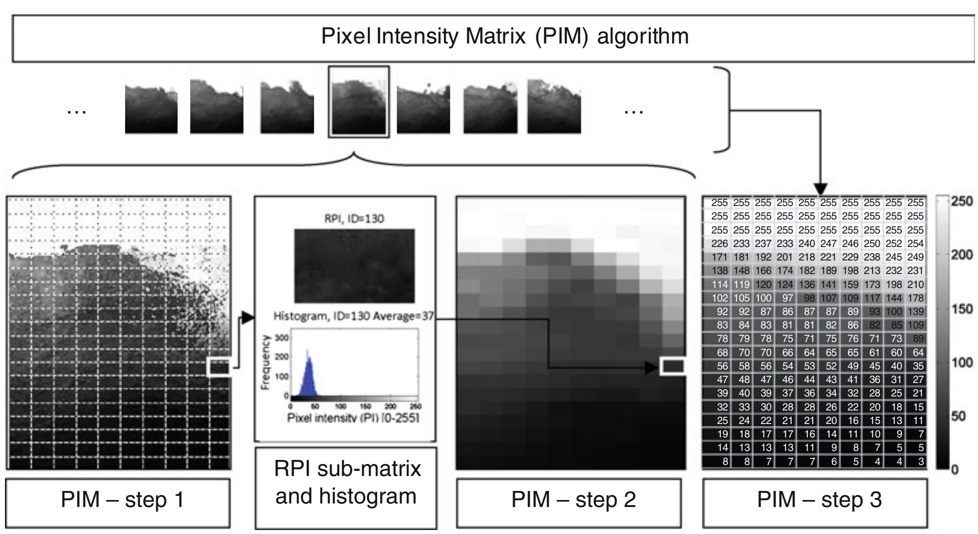

Fig. 4 Definition of the three steps in the Pixel Intensity Matrix algorithm: PIM—step 1 (resize matrix with $q = 20$ and $p = 10$), PIM—step 2 (Calculate the average matrix), and PIM—step 3 (calculate the average matrix over time)

pixel intensity matrix for each image, and PIM-step 3 calculates the time average pixel intensity matrix. Figure 4 illustrates the three steps that will now be explained in more detail.

3.2.1 PIM—step 1

In this step, the transformed image obtained in the previous algorithm, that is, the *PI*a ($m \times n$) matrix, is split into m/p times n/q smaller matrices, where p and q are integers and factors of m and n (Fig. 4 uppermost left image). A new matrix *RPI* is formed made up of these smaller matrices with dimensions $(p \times q)_{(m/p \times n/q)}$, such that $RPI(:,:)_{i,j}$ is the (i, j)th submatrix of *RPI*.

3.2.2 PIM—step 2

From each $RPI(:,:)_{i,j}$ matrix, an histogram of pixel intensity is obtained and the average occurrence is returned to an Average Matrix *AvPI* (Fig. 4 second image from left). The *AvPI* is an ($p \times q$) matrix such that *AvPI*(i, j) is calculated as the average pixel intensity of the (i, j)th submatrix of *RPI* (Fig. 4, third image from left). This procedure follows closely the work of Mossa and Tolve (1998), where the average value is also retained from the pixel intensity histogram. However, whereas Mossa and Tolve (1998) averaged the pixel intensity over the entire vertical profiles, we retain herein both horizontal and vertical average values.

3.2.3 PIM—step 3

The last step calculates the time average matrix *AvPIt*. The *AvPIt* is a ($p \times q$) matrix calculated as the time average pixel intensity of all *AvPI* matrices obtained in the previous step for a given test. The right image in Fig. 4 shows an example of that matrix. Each pixel intensity is represented in a gray scale by the color bar on the right and can be translated to a numerical value from 0 to 255. Hence, several vertical profiles of pixel intensity can now easily be retrieved as the columns in the *AvPIt* matrix.

The next section will describe the application of the image processing procedure to a typical hydraulic jump for two different flow rates at 3 different locations and discuss the air concentration results obtained with the new procedure.

4 Test results and validation

4.1 Experimental facility

The tests were carried for two inflow Froude numbers, and the measurements were conducted at three different longitudinal locations (Table 1). The two cases provided six sets of data (referred to as tests). One was used for calibration and the other five for validation. A series of at least 60 images per test were taken, that is, a data collection period of approximately 11.0 s. 60 images represent six times more data than what is referred to in previous studies, for example, Mossa and Tolve (1998) (see Introduction). Thus, it is considered sufficient for characterizing the average values presented in the void fraction profiles. Nonetheless, if a more robust frequency analysis is sought, this number should be increased, and the use of high-speed video camera might be preferred to the use of high-shutter speed photographic camera. All images have been previously cropped to 800 × 960 pixel dimensions (size 200 × 240 mm) around the three locations where measurements with the dual-tip conductivity probe were taken.

To enable a valid comparison, the level of resolution in the PIM algorithm was set to have a similar sampling band height used by the probe (i.e., the number of points of each vertical profile). Thus, the factors p and q in PIM-step 1 were set to 10 and 20 pixels, respectively, resulting in a resolution grid with 80×48 pixels (i.e., $\Delta y \times \Delta x$ the size of each $RPI(:,:)_{i,j}$ matrix). Smaller values of q had a similar profile, while larger values were (as expected) moving toward the averaging of the whole profile.

Although the tests were conducted with partially developed (PD) inflow conditions, the image processing procedure should be applicable regardless of the type of flow regime, given the similarities found in the literature between air concentration profiles (Takahashi and Ohtsu 2009).

4.2 Calibration

The image processing procedure was calibrated by selecting the vertical profile at $x - x_1 = 0.15$ m for $Fr_1 = 4.4$. Different values for the parameters (*Ptr* and *Ptr*2) in the IE algorithm were manually tested, until a good visual fit was obtained. In Fig. 3, the effect of the algorithm on the images is clearly shown. The *Smf* function in Eq. 5 in IE-step1 is responsible for darkening the image, while Eq. 7 in IE-step 2 eliminates the air bubbles attached to the glass sidewall. Equations 8 and 12 provide the necessary smooth transition between the area above and below the water surface. As previously discussed, the location of the water surface is not straightforward; hence, a transition area was

Table 2 Summary of the calibrated parameters used in the image processing procedure

$x - x_1$ (m)	*Ptr* (pi)	*Ptr*2 (pi)	*limSt* (i)	*limS* (i)
0.15	10	105	600	400
0.30	10	105	600	400
0.45	10	105	400	300

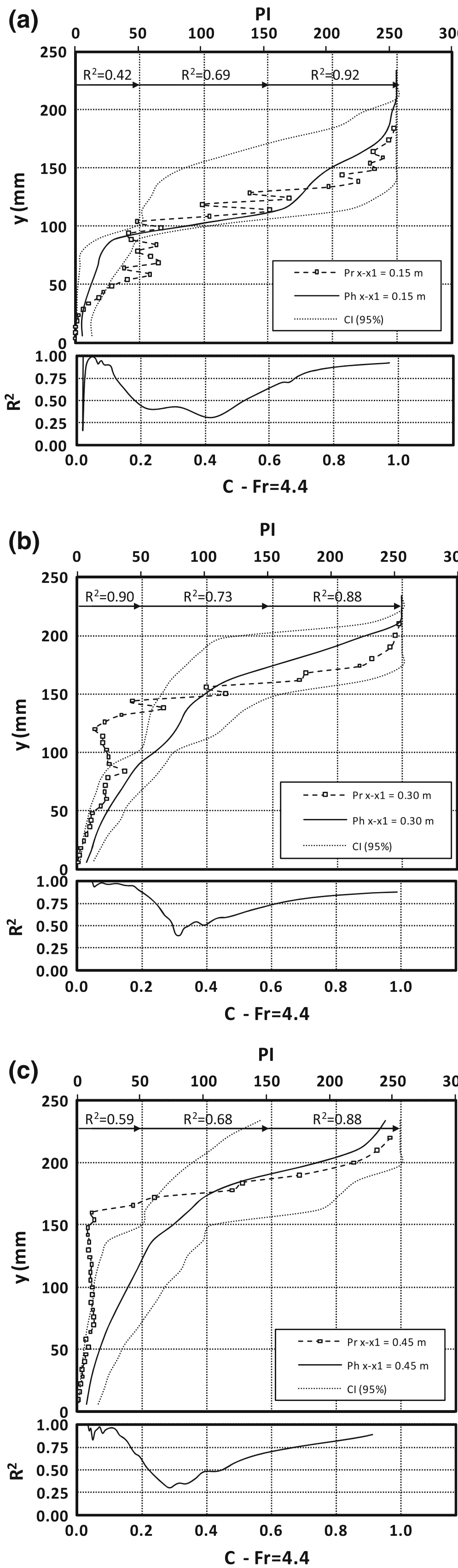

Fig. 5 Vertical profiles of air concentration in hydraulic jumps using dual-tip conductivity probes (Pr), vertical profiles of pi with 95% confidence intervals (CI), and square root of correlation coefficient (R^2) obtained with *AvPIt* applying the image processing procedure (Ph) for $Fr = 4.4$: **a** Test T1.1, **b** test T1.2, **c** test T1.3

adopted with varying limits (*limSt* and *limS*) depending on the longitudinal location ($x - x_1$). Table 2 summarizes the calibration parameters with best fitting results.

4.3 Validation

To validate the image processing procedure, the vertical profiles of pixel intensity (*AvPIt* columns) are compared with the air concentration profiles measured with the conductivity probes. Figures 5 and 7 show the comparison for $Fr = 4.4$ and $Fr = 5.1$ at $x - x_1(m) = \{0.15, 0.30, 0.45\}$. The vertical axis is the vertical elevation (mm), the top horizontal axis is the pixel intensity (pi), and the bottom horizontal axis is the air concentration (C). The horizontal axis limits have been changed according with the assumption that C can be estimated based on pi, such as a

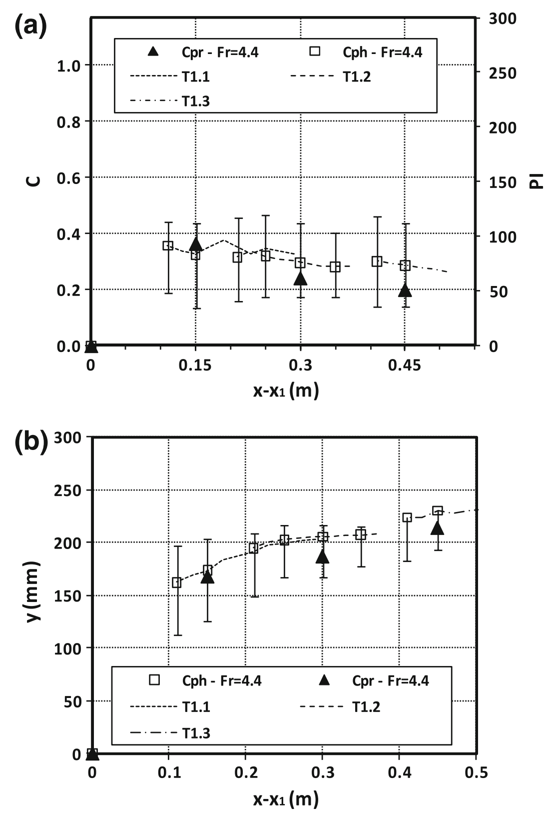

Fig. 6 Depth-averaged air concentration (**a**) and mean water surface level (**b**) for $Fr = 4.4$ (test T1.1–T1.3). Continuous measurements along the longitudinal direction of the hydraulic jump using the image processing procedure (*doted line* T1.1, *dashed line* T1.2, *dash-dot line* T1.3), local measurements using the dual-tip conductivity probes (Pr, *triangle*), and the image processing procedure (Ph, *square*) with *error bars* (confidence intervals 95%)

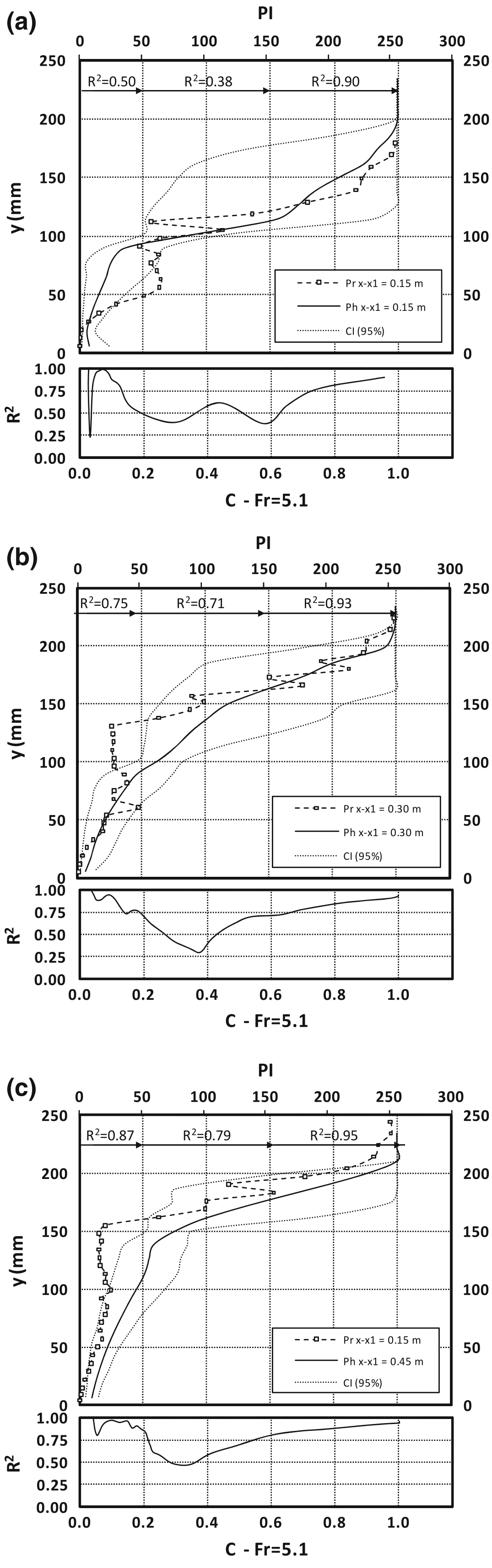

◀ **Fig. 7** Vertical profiles of air concentration in hydraulic jumps using dual-tip conductivity probes (Pr), vertical profiles of pi with 95% confidence intervals (CI), and square root of correlation coefficient (R^2) obtained with *AvPIt* through the image processing procedure (Ph) for $Fr = 5.1$: **a** Test T2.1, **b** test T2.2, **c** test T2.3

pi equal to 255 provides a C equal to 1 (100%). All profiles show the 95% confidence intervals (CI) of the vertical profiles and the square root of the correlation coefficient (R^2). As discussed earlier, the image processing procedure was calibrated to fit the profile at $x - x_1 = 0.15$ m with $Fr = 4.4$; hence, the other five profiles serve the purpose of validating the calibration.

Figures 6 and 8 show the depth-averaged pixel intensity (pi) and depth-averaged air concentration (*AvPIt* average columns) as well as the water surface level for $Fr = 4.4$ and $Fr = 5.1$, respectively. In air–water flow, the average air concentration is conventionally defined by Eq. 14:

$$C = \frac{1}{Y_{90}} \int_{0}^{Y_{90}} c\mathrm{d}y \tag{14}$$

where Y_{90} corresponds to the depth with air concentration equal to 90% (Chanson 1997; Wood 1991). While the water surface level was identified by an air concentration value of 0.90 in the profiles recorded with the conductivity probes, and the same location was identified by the equivalent pi = 230 = 255 × 0.90 in the profiles obtained in the image processing procedure. The value 230 was validated by comparing the two measured profiles shown in Figs. 6 and 8. The effect of changing this value will be discussed in the next subsection.

4.4 Time series results

Once the image processing procedure has been validated, it can be used to produce time series results of: complete vertical air concentration profiles, air concentration at specific depths, and surface water levels. Figures 9 and 10 present the time variations of the instantaneous readings collected at 5.2 fps for $Fr_1 = 4.4$ and $x - x_1 = 0.15$ m. Unlike the conductivity probe measurements, the visualization technique provides simultaneously the air concentration at different locations. It is, hence, possible to obtain complete instantaneous profiles of air concentration, as well as air concentration series, everywhere in the hydraulic jump as a function of x, y, or t. Figure 9 illustrates that advantage by plotting the isoclines of air concentration as a function of time.

The water surface was identified by linear interpolation of the vertical profiles of pixel intensity for the conventional value of 230. In Fig. 9, the water surface is characterized by three lines, where the two outer lines are

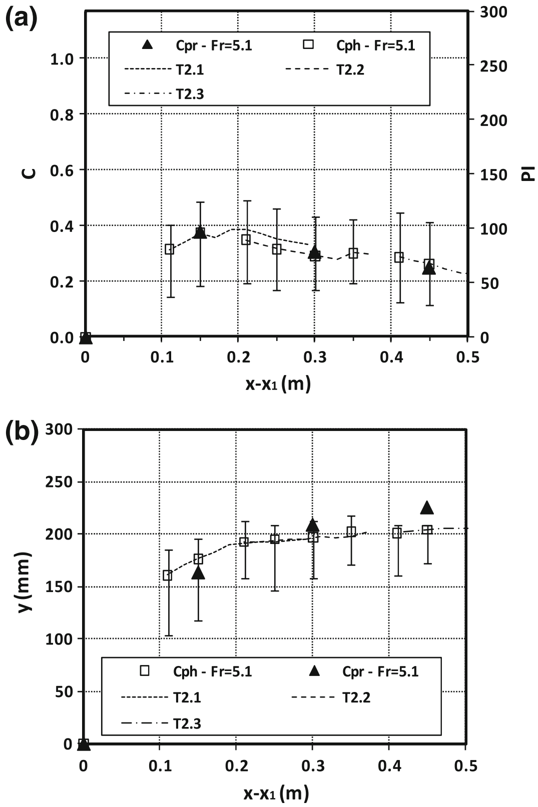

Fig. 8 Depth-averaged air concentration (**a**) and mean water surface level (**b**) for $Fr = 5.1$ (test T2.1–T2.3). Continuous measurements along the longitudinal direction of the hydraulic jump using the image processing procedure (*doted line* T2.1, *dashed line* T2.2, *dash-dot line* T2.3), local measurements using the dual-tip conductivity probes (Pr, *triangle*), and the image processing procedure (Ph, *square*) with *error bars* (confidence intervals 95%)

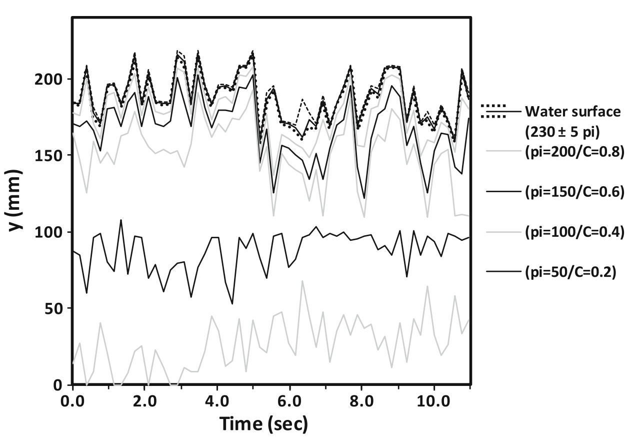

Fig. 9 Water surface level and pixel intensity/air concentration time series at different depths for $Fr = 4.4$ and for $x - x_1 = 0.15$ m, collected at 5.2 fps

interpolated lines using a pixel intensity of 235 and 225. Little difference is seen between the three water surface lines. All lines follow a similar trend, and the difference between the lower and center line has an average of 1.3 pi and standard deviation of 0.7 pi, while the difference between the upper and center line has an average of 1.1 pi and SD of 0.5 pi.

4.5 Discussion

The underling hypothesis of the present technique is that concentration (C) is proportional to the image pixel intensity (pi). Both vertical profiles obtained using the conductivity probe and the image processing procedure (IPP) show two distinct regions in the hydraulic jumps, the turbulent shear region and the upper region, as previously indicated by other researchers (Chanson 2007; Murzyn et al. 2005). While the turbulent shear region shows a steeper profile with lower air concentration (C), the upper region shows a shifting point where C shows a slight decrease before increasing drastically (Figs. 5, 7). All profiles show a similar trend across the vertical range. The $R^2 = 0.92$ obtained with T1.1 data used for calibration of the IPP shows a marginally better fit than T1.2 and T1.3 both with $R^2 = 0.88$; and a lower fit than T2.2 and T2.3 with $R^2 = 0.93$ and $R^2 = 0.95$, respectively. The shifting point (referred to earlier) is well predicted by the IPP, although it does show a smoother transition than the conductivity probe data. This is identified by the lower R^2 values in the range of $20\% < C < 40\%$. Nonetheless, outside that range, the conductivity probe and the IPP show a good agreement, particularly in the upper region.

The depth-averaged air concentration obtained with the IPP shows a good agreement with the conductivity probe measurements (Figs. 6, 8). The earlier study of Mossa and Tolve (1998) obtained similar good correlation between those two parameters, but Mossa and Tolve did not obtained complete vertical profiles and relied on a theoretical expression for determining the average air concentration. The agreement between the present conductivity probe and IPP results for the mean water surface level shows some improvement with increasing distance from the jump toe. This could be explained by the decrease in water surface oscillations as the flow turbulence decreases and the more likely homogeneous nature of the air–water flow as the measurement location moves away from the jump toe.

Light exposure is a critical issue to the proposed visualization technique that needs to be addressed; otherwise, differences may arise by a particular site light exposure or by using a different set of photos in the same location. To overcome that practical issue, first a calibration of the IPP is applied to all images in order to account for a particular site light exposure, after black surfaces are placed at the back of the experiment to remove glass reflections (Fig. 2), and finally the camera is switched to manual mode to assure the same light exposure in all images. The good overlapping of average air concentration in Figs. 6a and 8a

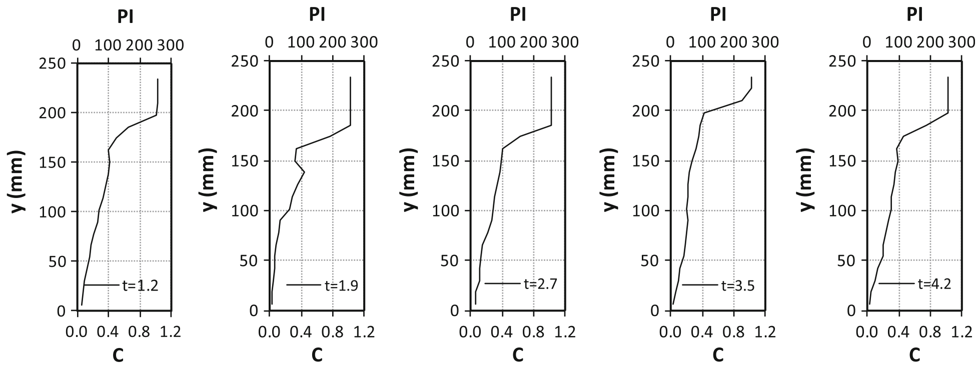

Fig. 10 Five complete air concentration vertical profiles at specific times for $Fr = 4.4$ and for $x - x_1 = 0.15$ m, collected at 5.2 fps

supports that the solution found is indeed effective in assuring equal light exposure.

The fact that the IPP measures close to the sidewall while the conductivity probe measures along the channel center line may contribute to some of the differences. Indeed, the readings obtained using the IPP are inevitably in the vicinity of the sidewall, and therefore, water depths at the center and at the channel sides will not coincide. On the other hand, changing the probe location to the same of the IPP readings cannot be accepted as a solution because it would stand to close to the side wall and inevitably interfere and enhance the sidewall effects. It is possible, nonetheless, to reduce that difference by using Eq. 7 to eliminate the air bubbles that remain attached to the glass wall that could cause an overestimation of the water depth (Fig. 3). The good overlapping of average surface water depth in Figs. 6b and 8b gives strength that the solution found contributes toward the minimization of those differences.

The time series results are possibly a major outcome of the image processing procedure. The new procedure allows the simultaneous measurements of complete time series of vertical air concentration profiles (Fig. 10) at several locations along the hydraulic jump. Although not the aim of this paper, a frequency analysis is a possible application of this method that would benefit from time series results; in that case, the coupling of this procedure with the use of high-speed video cameras is strongly suggested to provide a high-resolution time series of concentration (Fig. 9) (Chanson 2007).

5 Conclusion

The results show that the proposed visualization technique can be a powerful tool to complement air–water flow data collected with intrusive probes. The assumption that the void fraction in a hydraulic jump can be estimated based on the pixel intensity was verified. The method can be calibrated to estimate void factions with minimum additional work. The image processing procedure provides the time series of vertical profiles of air concentration everywhere within the photo window and with respect to x, y, or t. Furthermore, being a non-intrusive method (unlike probe readings), the image processing procedure allows the gathering of simultaneous measurements at different locations along the hydraulic jump without affecting the flow.

Despite the solid agreement in terms of time-averaged water depth values, the vertical profiles of time-averaged air concentration are expected to be more representative in the vicinity of the glass wall than at the center of the flume. While sidewall effects might explain some differences between the results obtained with the image processing procedure and the intrusive probe readings, solutions to some practical issues related with light exposure are provided: first, the calibration of the image processing procedure can be used to minimize light exposure subtleties that are dependent on a specific site conditions (e.g., type of light and direction); second, light reflections on the glass can be minimized by providing black surfaces at the background; and third, the light exposure of the images can be kept constant by setting the camera to full manual control during the shooting sequence. Finally, it is expected that the bubbles outside the limited DOF have insignificant influence to the results because, despite all being imaged, their intensity is much weaker than the bubbles inside the DOF.

Future work will include the use of the image processing procedure coupled with high-speed video camera to perform frequency analysis covering the entire hydraulic jump.

Acknowledgments The first and second authors acknowledge the support of the Foundation for Science and Technology, the *Operacional Temático Factores de Competitividade* (COMPETE) program, and the *Fundo Europeu de Desenvolvimento Regional* (FEDER) through project PTDC/AAC-AMB/101197/2008. The authors wish to acknowledge the anonymous reviewers for their helpful comments.

References

Bezdek JC, Keller J, Krisnapuram R, Pal NR (1999) Fuzzy models and algorithms for pattern recognition and image processing. Kluwer Academic Publishers, USA

Carvalho RF (2002) Hydrodynamic actions in hydraulic structures: numerical model of the hydraulic jump. PhD thesis, University of Coimbra, Portugal (in Portuguese)
Carvalho RF, Lemos CM, Ramos CM (2008) Numerical computation of the flow in hydraulic jump stilling basins. J Hydraul Res IAHR 46:739–775
Chachereau Y, Chanson H (2011) Bubbly flow measurements in hydraulic jumps with small inflow Froude numbers. Int J Multiph Flow 37:555–564. doi:10.1016/j.ijmultiphaseflow.2011.03.012
Chanson H (1997) Air bubble entrainment in free-surface turbulent shear flows. Academic Press, London, p 401
Chanson H (2007) Bubbly flow structure in hydraulic jump. Eur J Mech B/Fluids 26:367–384
Chanson H, Brattberg T (2000) Experimental study of the air-water shear flow in a hydraulic jump. Int J Multiph Flow 26:583–607
Chanson H, Carosi G (2007) Turbulent time and length scale measurements in high-velocity open channel flows. Exp Fluids 42:385–401
Davoust L, Achard JL, Hammoumi ME (2002) Air entrainment by a plunging jet: the dynamical roughness concept and its estimation by a light absorption technique. Int J Multiph Flow 28:1541–1564
Kucukali S, Chanson H (2008) Turbulence measurements in hydraulic jumps with partially-developed inflow conditions. Exp Therm Fluid Sci 33:41–53
Lennon JM, Hill DF (2006) Particle image velocity measurements of undular and hydraulic jumps. J Hydraul Eng ASCE 132:1283–1294
Long D, Steffler P, Rajaratnam N (1990) LDA study of flow structure in submerged hydraulic jump. J Hydraul Res IAHR 28:437–460
Mccorquodale JA, Khalifa A (1983) Internal flow in hydraulic jumps. J Hydraul Eng ASCE 109:684–701
Misra SK, Thomas M, Kambhamettu C, Kirby JT, Veron F, Brocchini M (2006) Estimation of complex air–water interfaces from particle image velocimetry images. Exp Fluids 40:764–775
Mossa M, Tolve U (1998) Flow visualization in bubbly two-phase hydraulic jump. J Fluids Eng 120:160–165
Mouaze D, Murzyn F, Chaplin JR (2005) Free surface length scale estimation in hydraulic jumps. J Fluids Eng 127:1191–1193
Murzyn F, Chanson H (2008) Experimental assessment of scale effects affecting two-phase flow properties in hydraulic jumps. Exp Fluids 45:513–521
Murzyn F, Chanson H (2009) Free-surface fluctuations in hydraulic jumps: experimental observations. J Fluids Eng 33:1055–1064
Murzyn F, Mouaze D, Chaplin J (2005) Optical fibre probe measurements of bubbly flow in hydraulic jumps. Int J Multiph Flow 31:141–154
Qingchao L, Drewes U (1994) Turbulence characteristics in free and forced hydraulic jumps. J Hydraul Res IAHR 32:877–898
Rajaratnam N (1962) An experimental study of air entrainment characteristics of the hydraulic jump. J Inst Eng India 42:247–273
Resch FJ, Leutheusser HJ (1972) Reynolds stress measurements in hydraulic jumps. J Hydraul Res IAHR 10:409–430
Resch F, Leutheusser H, Alemum S (1974) Bubbly two-phase flow in hydraulic jump. J Hydraul Div ASCE 100:137–149
Ryu Y, Chang K-A, Lim H-J (2005) Use of bubble image velocimetry for measurement of plunging wave impinging on structure and associated greenwater. Meas Sci Technol 16:1945–1953
Sarode MV, Ladhake SA, Deshmukh PR (2008) Fuzzy system for color image enhancement. World Acad Sci Eng Tech 48:311–316
Takahashi M, Ohtsu I (2009) Effect of inflow condition on air entrainment characteristics in hydraulic jump. In: 33rd IAHR congress, Vancouver, BC, Canada, 9–14, August, 2009
Vorobel R, Berehulyak O (2006) Gray image contrast enhancement by optimal fuzzy transformation, vol 4029. Springer, Berlin, pp 860–869. doi:10.1007/11785231
Wood I (1991) Air entrainment in free-surface flows. IAHR hydraulic structures design manual no. 4, hydraulic design considerations. Balkema, Rotterdam, p 149